Inorganic Chemistry

Article

Structure and Spin-Glass Magnetism of the $Mn_xNi_2Zn_{11−x}$ Pseudobinary γ-Brasses at Low Mn Contents

Sivaprasad Ghanta, Anustoop Das, Partha Pratim Jana,* Stanislav Vrtnik, Darja Gačnik, Jože Luzar, Andreja Jelen, Primož Koželj, Magdalena Wencka, and Janez Dolinšek*
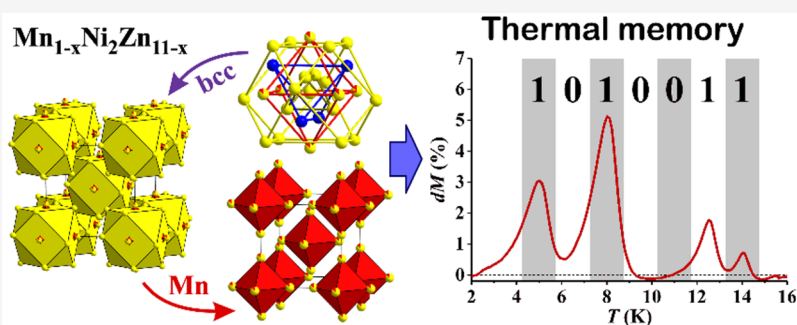
Read Online

ACCESS | Metrics & More | Article Recommendations

ABSTRACT: The pseudobinary $Mn_xNi_2Zn_{11−x}$ γ-brass-type phases at low Mn dopant levels ($x = 0.1−0.5$) were investigated. Crystal structures were determined for the two loading compositions of $x = 0.3$ and 0.5. The structures were solved in the cubic space group of $I\bar{4}3m$ and are described in close analogy to the Ni_2Zn_{11} parent γ-brass that is based on the 26-atom cluster, consisting of inner tetrahedron (IT), outer tetrahedron (OT), octahedron (OH), and cuboctahedron (CO). The refined site occupancies of the $Mn_xNi_2Zn_{11−x}$ ($x = 0.3, 0.5$) reveal that the cluster center, which is empty in the Ni_2Zn_{11}, shows a partial occupation by Zn, with a partial depletion of Zn at the IT sites. The OH sites show a mixed Zn/Mn occupation. The OT and CO sites remain intact with respect to Ni_2Zn_{11}. Magnetic properties were studied for the $Mn_{0.3}Ni_2Zn_{10.7}$ composition. The temperature-dependent zero-field-cooled and field-cooled magnetization, the ac susceptibility, the $M(H)$ hysteresis curves, the thermoremanent magnetization, and the memory effect demonstrate typical broken-ergodicity phenomena of a magnetically frustrated spin system below the spin freezing temperature $T_f \approx 16$ K. The $Mn_{0.3}Ni_2Zn_{10.7}$ γ-brass phase classifies as a spin glass, originating predominantly from the random distribution of diluted Mn moments on the octahedral partial structure.

1. INTRODUCTION

Complex metallic alloys (CMAs) are a class of intermetallic compounds that possess giant unit cells comprising from several tens up to many thousands of atoms arranged in well-defined atomic clusters of different polyhedral symmetry.[1,2] CMA structures possess various types of disorder, including configurational disorder due to a statistically varying orientation of a particular subcluster, chemical (substitutional) disorder, partial site occupation (occupancy smaller than 1), and split occupation, where two neighboring sites are alternatively occupied because they are too close in space. Many CMAs possess a solid-solution range, so that the composition of a single phase can be varied. The category of CMAs includes the family of γ-brasses, containing 52 atoms in the unit cell.[3] The structure of γ-brass-type phases is described in terms of a 26-atom cluster, made up of four successive shells. Starting from the empty cluster center (CC), the first shell is the inner tetrahedron (IT), followed by outer tetrahedron (OT), octahedron (OH), and cuboctahedron (CO). On the

basis of the space group, γ-brasses are divided into four families:[3] (1) I-cell-type γ-brasses with space group $I\bar{4}3m$ form a body-centered cubic (bcc) lattice with two identical 26-atom clusters in the unit cell, centered at the highly symmetric positions (0,0,0) and (1/2,1/2,1/2), (2) P-cell type with space group $P\bar{4}3m$ adopt a CsCl structure composed of two different 26-atom clusters, (3) F-cell type with space group $F\bar{4}3m$ form superstructures, and (4) R-cell type with space group $R3m$ (a subgroup of $P\bar{4}3m$) are rhombohedral. The I-cell and P-cell types are the most numerous ones, found in 24 binary alloy systems.[3]
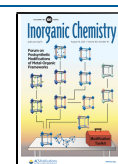
Binary γ-brasses were widely investigated in the past, both experimentally and theoretically, and the state of the art in the field is summarized in the book by Mizutani.[3] Within the finite solid solution range of the γ-brass phase, the stoichiometric compositions can adopt one of the A_2B_{11}, A_4B_9, A_5B_8, A_7B_6, and $A_{10}B_3$ formulas with space group $I\bar{4}3m$ and a combination of these two with space group $P\bar{4}3m$. According to the classification in terms of a combination of constituent elements in the periodic table, the I- and P-cell γ-brasses are divided into three groups. Group I comprises 11 combinations of a monovalent noble metal (Cu, Ag) and a polyvalent element, whose valency is well-defined. Group II also includes 11 γ-brasses, which consist of 3d transition-metal elements like TM = V, Mn, Fe, Co, and Ni and either divalent elements Be, Zn, Cd or trivalent elements Al, In. Group III includes γ-brasses consisting of a combination of two nontransition metal elements like Ag, Li, and Pb.

The γ-brass phases belong to the class of Hume−Rothery phases, where the crystal structure achieves stability at a specific valence electron concentration of e/a.[3−7] A pseudogap in the electronic density of states (DOS) is formed at the Fermi energy ε_F, which efficiently lowers the kinetic energy of the conduction-electron system, making the structure more stable. γ-Brasses from the group I are stabilized at the value e/a = 21/13 = 1.615. For the group II, the situation is less clear, because the e/a value for the TM is not a-priori known. Theoretical band calculations using the Full-Potential Linearized Augmented Plane Wave (FLAPW) method applied to the stoichiometric TM_2Zn_{11} (TM = Fe, Co, Ni, Pd) γ-brasses from the group II have yielded e/a values between 1.70 and 1.80,[6] which is considered still acceptable to claim that the stability of these alloys follows the Hume−Rothery electron concentration rule. The γ-brass phase field for the TM_2Zn_{11} family is extended over 15−30 atom % of the TM element.

Inspired by the knowledge and understanding of the stabilization mechanism of binary γ-brasses, the research has been extended to ternary γ-brass phases. New pseudobinary/ternary γ-brass phases were unraveled in the Co−Pd−Zn,[8] Fe−Pd−Zn,[9] and Ni−Zn-X (X = In, Ga)[10] systems, starting from the knowledge of electronic structures of the binary Co_2Zn_{11}, Fe_2Zn_{11}, Pd_2Zn_{11}, and Ni_2Zn_{11}. The Co−Pd−Zn and Fe−Pd−Zn ternary compounds show weak ferromagnetic or ferrimagnetic behavior, unlike their binary parent compounds. Recently, the phase diagram of the ternary Mn−Ni−Zn system has been studied.[11,12] Three new ternary compounds, denoted as T, τ_1, and τ_1, were found to exist at 400 °C, and extended single-phase regions of the phases Mn_5Zn_{21}, Ni_2Zn_{11}, $NiZn_3$, and NiZn were observed. In this work, we investigate experimentally the γ-brass-type Mn−Ni−Zn pseudobinary/ternary phases based on the Ni_2Zn_{11} parent compound.[13] By introducing Mn as a dopant to the Ni_2Zn_{11}, the atomic radius of Mn (r_{Mn} = 127 pm) is closer to Zn (r_{Zn} = 134 pm) than Ni (r_{Ni} = 124.6 pm). The Pauling electronegativity of Mn (1.55) is also closer to Zn (1.65) than Ni (1.91). For those reasons it can be assumed that Mn will preferentially substitute for Zn. Here we concentrate on the system $Mn_xNi_2Zn_{11-x}$ at low Mn dopant levels (x = 0.1−0.5), by determining the crystallographic structure for two nonstoichiometric compositions and the physical properties, with the emphasis on magnetism.

2. RESULTS

2.1. Structure Determination and Description.
The materials, synthesis, and characterization by powder X-ray

diffraction (PXRD), single-crystal X-ray diffraction (SCXRD), and energy-dispersive X-ray spectroscopy (EDS) are detailed in the Experimental Section. The phase purity of the samples was verified by PXRD and Rietveld refinement plots, confirming that the entire series of the $Mn_xNi_2Zn_{11-x}$ (x = 0.1−0.5) compounds were single-phase, belonging to the γ-brass-type phase $I\bar{4}3m$.

The PXRD spectra and the Rietveld refinement plots for the loading compositions $Mn_{0.3}Ni_{2.0}Zn_{10.7}$ (C1) and $Mn_{0.5}Ni_{2.0}Zn_{10.5}$ (C2) are shown in Figure 1 with the goodness
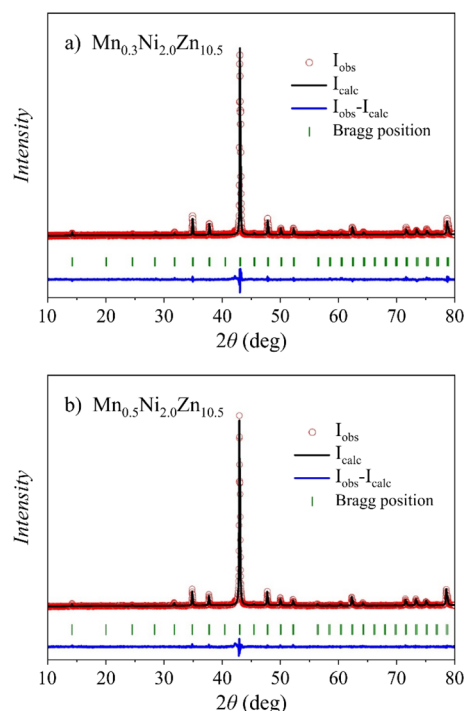
Figure 1. Powder XRD spectra and Rietveld refinement plots for the loading compositions (a) $Mn_{0.3}Ni_{2.0}Zn_{10.7}$ (GOF = 1.34, R_{all} = 5.58, wR_{all} = 5.86) and (b) $Mn_{0.5}Ni_{2.0}Zn_{10.5}$ (GOF = 1.30, R_{all} = 2.95, wR_{all} = 3.20).

of fit (GOF) indicated. The crystal structures were subsequently determined by SCXRD for these two compositions. The complete crystallographic data are presented in Table 1 (additional crystallographic information is available regarding the Accession Codes), whereas the final atomic coordinates, site occupancies, and isotropic displacement parameters are given in Table 2.

The crystal structures were solved in the cubic space group $I\bar{4}3m$ (No. 217). The structure solution has generated four crystallographically independent positions in the unit cell. The preliminary stage of refinement for the crystal C1 converged at the $R(F)$ value of 4.8%. It was challenging to identify the exact atomic positions of Ni and Zn in the crystal structure on the basis of electron density due to their very similar X-ray scattering factors. Thus, at this stage, the positions of Ni and Zn were allocated based on the model established for ordered γ-brass type Ni_2Zn_{11}.[14,15] Of the four crystallographic sites, one 8c site was assigned to Ni, whereas the remaining three (8c, 12e, 24g) were assigned to Zn, and the subsequent refinement converged at the $R(F)$ value of 4%. The 12e site discerned a relatively larger isotropic atomic displacement parameter (ADP) of ~0.021 Å^2 with respect to the average value. An

Table 1. X-ray Crystallographic Data for the Crystals of Loading Compositions $Mn_{0.3}Ni_{2.0}Zn_{10.7}$ (C1) and $Mn_{0.5}Ni_{2.0}Zn_{10.5}$ (C2)

	C1	C2
chemical formula	$Mn_{1.56(10)}Ni_8Zn_{41.54(3)}$	$Mn_{1.96(7)}Ni_8Zn_{41.55(2)}$
chemical formula (atom %)	$Mn_{3.05}Ni_{15.66}Zn_{81.29}$	$Mn_{3.81}Ni_{15.53}Zn_{80.66}$
EDS formula (atom %)	$Mn_{3.3(1)}Ni_{14.81(1)}Zn_{81.9(1)}$	$Mn_{3.5(1)}Ni_{15.0(2)}Zn_{81.5(2)}$
loading composition (atom %)	$Mn_{2.31}Ni_{15.38}Zn_{82.32}$	$Mn_{3.85}Ni_{15.38}Zn_{80.77}$
Pearson symbol	$cI{\sim}51$	$cI{\sim}52$
crystal system	cubic	
space group; Z	$I\bar{4}3m$ (217); 1	
a, Å	8.9420(2)	8.9628(2)
V, Å^3	715.00(3)	720.00(3)
ρ_{calc}, g cm^{-3}	7.597	7.590
μ, mm^{-1}	39.811	39.681
crystal color	silvery with metallic luster	
data collection	four-circle diffractometer	
diffractometer	Bruker Photon II	
radiation; wavelength, Å	Mo Kα; 0.71073	
monochromator	graphite	
T, K	293	
$\theta_{min} - \theta_{max}$, deg	3.22−30.39	3.21−30.51
reflns measured	12 933	9178
index range	$-12 \leq h \leq 12$ $-12 \leq k \leq 12$ $-12 \leq l \leq 12$	$-12 \leq h \leq 12$ $-12 \leq k \leq 12$ $-12 \leq l \leq 12$
data reduction/ abs correction	multiscan	
crystal size, mm	0.08 × 0.04 × 0.02	0.1 × 0.08 × 0.02
unique reflns	229	234
R_{int}	0.0618	0.0628
structure solution/ refinement	JANA2006 package program	
structure solution	Superflip	
No. reflns used	229	234
No. variables	22	22
observed reflns ($I > 3\sigma(I)$)	226	230
$R(F^2 > 3\sigma(F^2))$	0.0236	0.0168
$R(F)$ (all data)	0.0241	0.0173
K^a	0.0004	0.0004
$wR(F^2)$ (all data)	0.0735	0.0454
GOF (all)	1.67	1.67
$\Delta\rho_{min}/\Delta\rho_{max}$ (e Å^{-3})	−0.59/2.25	−1.48/0.56

^{a}Weighting scheme based on measured standard uncertainty $w = 1/(\sigma 2(I) + kI2)$.

independent refinement of the 12e site assigned as Zn resulted in a site occupancy factor (SOF) lower than unity, whereas the site assigned as Mn led to the occupancy (SOF) higher than unity. Hence, the 12e site was modeled by partially replacing Mn for Zn (Zn2/Mn2) assuming these sites to be fully occupied overall. The subsequent refinement resulted in the $R(F)$ value of 3.5%. The 8c site occupied by Zn also discerned a slightly larger isotropic ADP ($\sim$0.018 Å^2) and was tested for partial occupancy. At this stage, additional residual electron density was identified at the 2a site in the cluster center (CC) located at (0.5, 0.5, 0.5) and included as Zn. The 2a (Zn) site

was also examined for partial occupancy, as the distance between the 2a and 8c sites is too short ($\sim$1.63 Å). The local structural disorder was modeled by introducing split positions. In no case does the sum of site occupancy factors (SOFs) of two such sites exceed unity, but the splits are explainable in terms of a set of locally ordered clusters. Both sites were independently refined, following the relation of SOF(Zn(CC)) + SOF(Zn(IT)) $\approx$ 1.00. The harmonic ADPs for all atoms including the isotropic extinction correction were taken into account at the final stage of the refinement, and the $R(F)$ value converged at 2.4%. The SCXRD refined model for the C1 crystal was used as the initial model for the refinement of the SCXRD data collected for the C2 crystal. The refined ($Z = 4$) compositions $Mn_{0.396}Ni_2Zn_{10.38}$ for the C1 and $Mn_{0.491}Ni_2Zn_{10.376}$ for the C2 were checked by EDS, and good matching was obtained (Table 1). Each structure (C1 and C2) was tested for possible twinning by an inversion and absolute configuration. The Flack parameters for C1 and C2 after the refinement resulted in −0.1(2) and −0.03(16), respectively. Hence, the structures are not twinned by an inversion. It is worth mentioning that these data were tentatively truncated to test for any trend in the occupancy of the Zn2/Mn2 site. No such trend was detected, that is, the data are stable toward a high-order truncation. An artificial truncation of the data to lower reciprocal space vectors resulted in similar values for the occupancy of the Zn2/Mn2 site.

The structure can be described in close analogy to the Ni_2Zn_{11} parent γ-brass compound, in which Ni occupies solely the 8c(OT) position with full occupancy, whereas the remaining three sites 8c(IT), 12e(OH), and 24g(CO) are fully occupied by Zn. The pseudobinary structures C1 and C2 adopt the same structure type, described by the 26-atom γ-cluster. The refined site occupancies for the C1 composition reveal that the central (CC) site, which is empty in the γ-cluster of the Ni_2Zn_{11}, is partially occupied by Zn (SOF(CC) = 0.107(13)) with a simultaneous depletion of Zn at the IT sites (SOF(IT) = 0.861(7)). The OH site shows a Zn/Mn substitutional disorder. The OT and CO sites that are occupied by Ni and Zn, respectively, remain unaffected by the Mn insertion. The structure for the C1 composition is shown in Figure 2. The five successive shells of the distorted γ-cluster are presented in Figure 2a, with the OH sites showing mixed Zn/Mn occupation of 0.87/0.13, whereas one complete γ-cluster is shown in Figure 2b. The bcc unit cell is shown in Figure 2c, whereas the magnetic lattice with diluted Mn spins on the OH sites (see later) is shown in Figure 2d. The partial structure of the partially populated CC and IT sites (both occupied by Zn) is shown in Figure 2e. The C2 crystal shows a similar occupancy pattern and crystal structure, where the occupancy of the CC site slightly decreases (SOF(CC) = 0.082(11)), with a further increase of Zn occupation at the IT sites (SOF(IT) = 0.913(5)).

2.2. Spin-Glass Magnetism of the γ-Brass Type $Mn_{0.3}Ni_2Zn_{10.7}$. Magnetic properties were studied via the magnetic experiments and the specific heat for the loading composition $Mn_{0.3}Ni_2Zn_{10.7}$(C1). The structure contains two kinds of magnetic elements, namely, Mn and Ni, where Mn is antiferromagnetic (AFM) as a pure metal, whereas Ni is ferromagnetic (FM). In an electrically conducting medium, the interaction between the moments is the conduction-electron mediated Ruderman−Kittel−Kasuya−Yosida (RKKY) indirect exchange, which oscillates in space on the scale of many

Table 2. Atomic Coordinates, Site Occupancies, and Equivalent Isotropic Displacement Parameters of $Mn_{0.3}Ni_{2.0}Zn_{10.7}$ (C1) and $Mn_{0.5}Ni_{2.0}Zn_{10.5}$(C2)

crystal	atom	Wyckoff	occupancy	x	y	z	U_{eq},[a] Å²
C1	Zn0	2a(CC)	0.107(13)	0.5	0.5	0.5	0.016(4)
C2			0.082(11)	0.5	0.5	0.5	0.030(6)
C1	Zn1	8c(IT)	0.861(7)	0.605 28(10)	0.394 72(10)	0.605 28(10)	0.0136(2)
C2			0.913(5)	0.605 20(7)	0.394 80(7)	0.605 20(7)	0.013 62(17)
C1	Ni1	8c(OT)	1	0.671 98(9)	0.328 02(9)	0.328 02(9)	0.009 16(19)
C2			1	0.671 83(6)	0.328 17(6)	0.328 17(6)	0.009 47(13)
C1	Zn2/Mn2	12e(OH)	0.87(3)/0.13	0.852 47(16)	0.5	0.5	0.0166(3)
C2			0.84(2)/0.16	0.853 20(11)	0.5	0.5	0.0144(2)
C1	Zn3	24g(CO)	1	0.954 96(9)	0.306 26(7)	0.306 26(7)	0.0163(2)
C2			1	0.955 83(7)	0.306 69(5)	0.306 69(5)	0.015 81(16)

[a]U_{eq}, Å² is defined as one-third of the trace of the orthogonalized U^{ij} tensor.
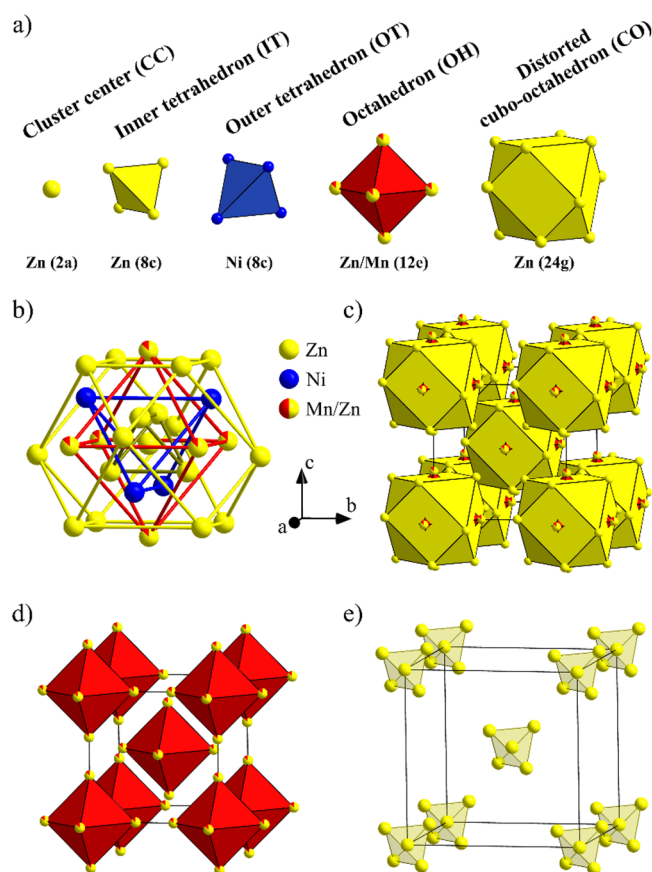
Figure 2. Crystal structure for the composition of $Mn_{0.396}Ni_2Zn_{10.38}$ (crystal C1). (a) Successive shells of the distorted γ-cluster, with the OH sites showing mixed Zn/Mn occupation of 0.87(3)/0.13; (b) one complete γ-cluster; (c) the bcc unit cell; (d) the octahedral partial structure, representing the magnetic lattice with diluted Mn spins on the OH sites, and (e) the tetrahedral partial structure, representing the positional disorder in the partially populated CC and IT sites (both occupied by Zn).

Temperature-Dependent Magnetization and Magnetic Susceptibility. The temperature-dependent zero-field-cooled (zfc) and field-cooled (fc) direct-current (dc) magnetization in a low magnetic field of $\mu_0 H = 5$ mT, measured in the temperature range of 300−1.8 K, is shown in Figure 3a. The
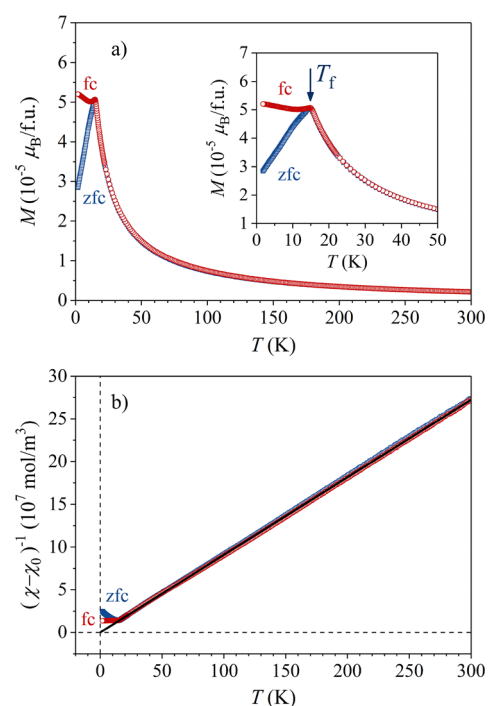
Figure 3. (a) Temperature-dependent zfc and fc dc magnetization in a magnetic field $\mu_0 H = 5$ mT (fu denotes formula unit, that is, one $Mn_{0.033}Ni_{0.148}Zn_{0.819}$ average "atom"). (inset) The transition region around the spin freezing temperature T_f on an expanded scale. (b) Magnetic susceptibility in a Curie−Weiss plot, where the solid line is the fit in the paramagnetic regime.

nanometers between positive and negative values, depending on the distance between the spins. Because of the random positioning of Mn on the octahedral partial structure (the Zn/Mn mixed-occupied OH site), both FM and AFM interactions are present, causing frustration of the magnetic subsystem. The disorder caused by a partial occupancy of the CC and IT sites adds to the frustration as well.

magnetization is given in Bohr magnetons μ_B per one $Mn_{0.033}Ni_{0.148}Zn_{0.819}$ average "atom" (i.e., per one formula unit (fu)). When cooled, a paramagnetic growth of the magnetization is observed down to 16 K, where M_{zfc} exhibits a cusp and decreases toward zero when further cooled, whereas M_{fc} stays approximately constant below that temperature. Such behavior is typical of a kinetic spin-freezing transition in spin glasses,[16] where the temperature of the M_{zfc} cusp is associated with the spin-freezing temperature T_f. Below T_f, the ergodicity of the spin system is broken; that is, the spin fluctuation times

become so long that the system cannot reach an equilibrium state on the accessible experimental frequency scale, which is the origin of the $M_{zf} - M_{fc}$ splitting.

The magnetic susceptibility $\chi = M/H$ in the paramagnetic phase ($T > T_f$) was analyzed by the Curie–Weiss law, $\chi = \chi_0 + C_{CW}/(T - \theta)$. Here C_{CW} is the Curie–Weiss constant, θ is the Curie–Weiss temperature, and χ_0 is the temperature-independent term of the susceptibility. χ_0 is a sum of the negative (diamagnetic) Larmor core susceptibility, the positive Pauli paramagnetic spin susceptibility of the conduction electrons, and the negative Landau susceptibility due to the conduction-electron orbital circulation in the magnetic field, where all three contributions are of the same order of magnitude. The Larmor susceptibility was estimated from literature tables[17] as $\chi_{Larmor} \approx -2 \times 10^{-10}$ m³ mol⁻¹. The fit yielded the value $\chi_0 = -6.6 \times 10^{-10}$ m³ mol⁻¹, which is of the correct order of magnitude. The plot of the susceptibility ($\chi - \chi_0$)⁻¹ vs T and the Curie–Weiss fit (solid line) are shown in Figure 3b. Excellent fit was obtained in the entire paramagnetic regime above $T_f \approx 16$ K. The mean effective Bohr magneton number $\bar{p}_{eff}$, obtained from[18] $\bar{p}_{eff} = (797.7\sqrt{\text{mol/m}^3\text{K}}) \times \sqrt{C_{CW}}$ has yielded the mean effective paramagnetic moment $\bar{\mu}_{eff} = \bar{p}_{eff}\mu_B = (0.84 \pm 0.05)\mu_B$. This value is strongly reduced with regard to the experimental paramagnetic free-ion values of localized ions Mn^{3+}, Mn^{2+}, Ni^{3+}, and Ni^{2+} that amount to 4.9, 5.9, 4.8, and 3.2 μ_B, respectively. On the basis of the Curie–Weiss analysis we are, however, unable to discriminate between a small number of magnetic ions with large magnetic moments and a large number of magnetic ions with small magnetic moments in the $Mn_{0.3}Ni_2Zn_{10.7}$ structure. Likewise, we are unable to discriminate between the magnetic moments of Mn and Ni.

The Curie–Weiss temperature was determined from the fit as $\theta = 0$ K (with an estimated error of ± 1 K). This temperature is generally an indication of the dominant type of interspin interactions, being either AFM ($\theta < 0$) or FM ($\theta > 0$). The $Mn_{0.3}Ni_2Zn_{10.7}$ 3d magnetic alloy is an exchange-dominated spin system, where the randomness of the Mn positioning on the magnetic sublattice introduces a distribution of the exchange coupling constants $\mathcal{J}$. The zero value of the Curie–Weiss temperature suggests that the distribution function $P(\mathcal{J})$ extends to both positive ($\mathcal{J} > 0$, FM coupling) and negative ($\mathcal{J} < 0$, AFM coupling) $\mathcal{J}$ values.[19] It also indicates that the average exchange interaction is close to zero, $\bar{\mathcal{J}} = 0$, which is characteristic of spin glasses. This supports that the magnetic state below $T_f \approx 16$ K is of a spin-glass type, where the AFM and FM interactions are both present in similar proportions.

The alternating-current (ac) magnetic susceptibility was measured between 300 and 1.8 K in a sinusoidal magnetic field of amplitude $\mu_0 H_0 = 0.2$ mT at logarithmically spaced frequencies between 0.1 and 1000 Hz. The real part of the susceptibility χ' is presented in Figure 4a, where a peak at ~16 K that shifts with frequency to higher temperatures is evident (the details are shown in Figure 4b). Such a frequency dependence indicates a spin-freezing transition from an ergodic to a nonergodic state. The frequency-dependent spin-freezing temperature $T_f(\nu)$ is conveniently defined as the temperature of the χ' peak, and the corresponding $T_f(\nu)/T_f(1 \text{ Hz})$ relation is shown in the inset of Figure 4b. The fractional shift of $\Delta T_f/T_f$ per log ν was determined as $\Gamma = \Delta T_f/T_f \Delta(\log \nu) = 6.1 \times$
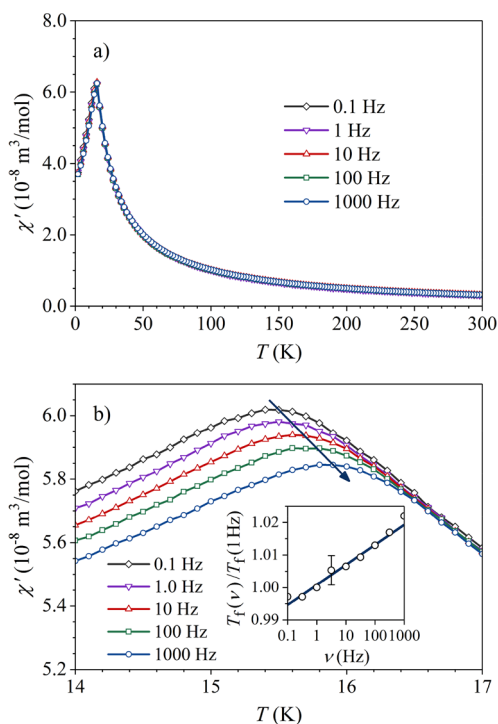
Figure 4. (a) Temperature- and frequency-dependent real ac susceptibility χ'. (b) The χ' peak on an expanded scale (the arrow marks the shift of the peak with frequency). (inset) The $T_f(\nu)/T_f(1 \text{ Hz})$ vs ν relation.

10^{-3}. This value falls into the range typical for spin glasses, where the values of Γ from 10^{-2} to 10^{-3} are common.[20]

The M(H) Magnetization. The $M(H)$ magnetization curves below 30 K are shown in Figure 5a. Hysteresis becomes noticeable below 10 K, where the coercive field at the lowest measured temperature of 2 K amounts to $\mu_0 H_c = 0.12$ T. The close-up field of the hysteresis loops is ~2 T. At large fields, the $M(H)$ curves approach asymptotically an inclined line.

The 10 K $M(H)$ curve, where the hysteresis is still absent, was theoretically reproduced by assuming a spin-glass-type distribution $P(\mathcal{J})$, shown schematically in the inset of Figure 5b. The curve was modeled by the function $M = M_0 L(x) + k\mu_0 H$. Here the term $M_0 L(x)$ corresponds to the $\mathcal{J} > 0$ (FM) side of $P(\mathcal{J})$, where $L(x)$ with $x = \mu\mu_0 H/(k_B T)$ is the Langevin function, and μ is the effective moment of the FM clusters. The term $k\mu_0 H$ corresponds to the $\mathcal{J} < 0$ (AFM) side of $P(\mathcal{J})$, with $\mu_0 k$ representing the AFM susceptibility. In the limit of large H, the total $M(H)$ curve approaches asymptotically an inclined line of the slope $\mu_0 k$.

The theoretical fit of the 10 K curve with the above model is presented in Figure 5b. The fit yielded the parameter values $M_0 = 1.2 \times 10^{-2}\mu_B/$fu, $\mu = 22\mu_B$, and $k = 2.6 \times 10^{-3}\mu_B/$(fuT). The small FM group moments of $22\mu_B$ suggest FM spin domains of a couple of nanometers in size. The fit qualitatively confirms the spin-glass-type $P(\mathcal{J})$ distribution with vanishing average exchange interaction, $\bar{\mathcal{J}} = 0$. This is in accord with the zero Curie–Weiss temperature.

Specific Heat. Specific heat is suitable for the characterization of phase transitions (structural, magnetic, superconducting), where an ordering of some degree of freedom takes place at the phase transition temperature. The energy of the ordered state is lower than the energy of the high-
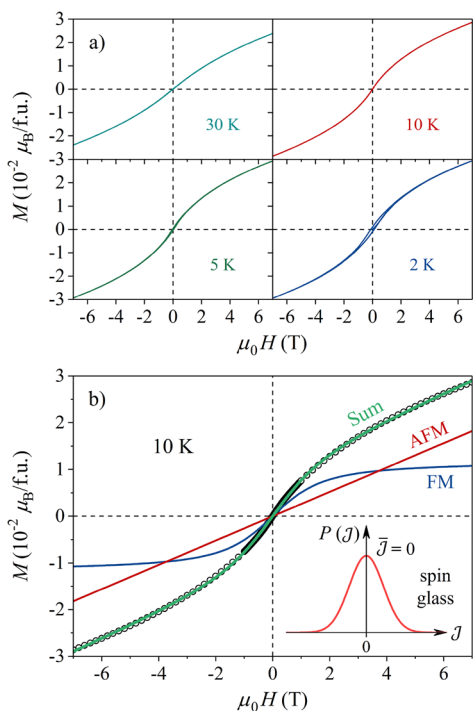
Figure 5. (a) $M(H)$ curves in the temperature range of 30−2 K. (b) The 10 K curve with the theoretical fit (see text), showing also the FM and AFM contributions separately. (inset) Schematic view of the $P(\mathcal{J})$ distribution for a spin glass ($\bar{\mathcal{J}} = 0$).


Figure 6. Specific heat $C(T)$ below 30 K in the magnetic field range of 0−9 T. Vertical arrow denotes the spin-freezing temperature $T_f = 16$ K, determined from the magnetic susceptibility. (inset) The specific heat below 9 K in a C/T vs T^2 plot.

temperature disordered state, so that the energy released upon ordering exits the system as a heat in the form of an exothermic peak. The low-temperature specific heat of a magnetic alloy can be written as $C = \gamma T + \alpha T^3 + C_m$, where γT, αT^3, and C_m are the electronic, lattice, and magnetic contributions, respectively. For canonical spin glasses (denoting a noble metal host like Cu or Ag with diluted magnetic impurities Fe, Mn, etc.), C_m usually exhibits a broad peak upon spin freezing, with the peak maximum located at $T_{max} \approx 1.4 T_f$.[21] The exothermic peak in the region of the spin-freezing temperature indicates that the spins adjust locally to their neighbors in an energetically favorable configuration to reduce the exchange energy, although no long-range magnetic ordering takes place. For a purely kinetic spin freezing transition, however, the spins or small spin clusters gradually freeze into random directions during continuous cooling, so that no heat is released at T_f, and the specific heat does not show any anomaly.

The specific heat of the Mn$_{0.3}$Ni$_2$Zn$_{10.7}$ γ-brass was determined in the temperature range of 1.8−300 K in magnetic fields between 0 and 9 T. The $C(T)$ graphs below 30 K are shown in Figure 6, where it is evident that there is no anomaly at the spin-freezing temperature $T_f \approx 16$ K, and the specific heat also does not show any field dependence. This is in favor of a kinetic spin-freezing transition from an ergodic to a nonergodic state. The specific heat below 10 K is presented in the inset of Figure 6 in a C/T versus T^2 plot, wherefrom the electronic specific heat coefficient was determined as $\gamma = 4.71$ mJ mol^{-1} K^{-2}. This value is almost the same as that reported for the Ni$_2$Zn$_{11}$ parent γ-brass ($\gamma = 4.5$ mJ mol^{-1} K^{-2}).[22] Since $\gamma = (\pi^2/3) k_B^2 g(\varepsilon_F)$ is directly proportional to the electronic DOS at the Fermi level $g(\varepsilon_F)$, this indicates that the DOS at ε_F of the Mn-doped Mn$_{0.3}$Ni$_2$Zn$_{10.7}$ is not changed much with respect to the Ni$_2$Zn$_{11}$. The lattice specific heat coefficient α
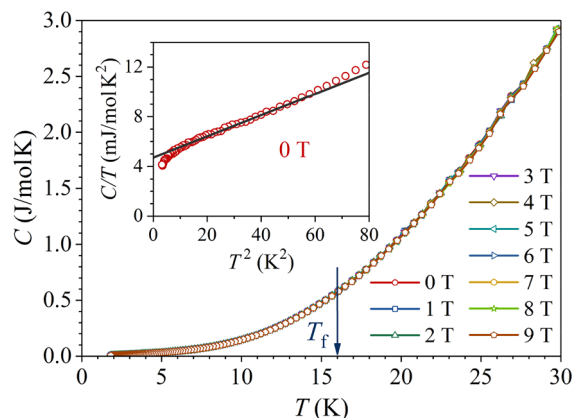
yielded the Debye temperature of $\theta_D = 283$ K (for comparison, the θ_D values of the constituent metals are $\theta_D^{Zn} = 329$ K, $\theta_D^{Ni} = 477$ K, and $\theta_D^{Mn} = 409$ K).

Thermoremanent Magnetization. The broken-ergodicity state of a spin glass (as well as of other magnetically frustrated systems) can be further characterized by measuring the time decay of the thermoremanent magnetization (TRM), which is logarithmically slow below the spin-freezing temperature T_f.[23−31] This reflects the slow approach of the spin system toward a thermal equilibrium, which cannot be reached on the available frequency scale of a given experimental technique due to a broad distribution of spin relaxation times. The TRM time-decay measurement protocol involves (1) continuous cooling of the spin system in a magnetic field H_{fc} through T_f into the nonergodic state, (2) stopping the cooling at a certain measuring (or aging) temperature $T_m < T_f$ for a waiting (aging) time t_w, (3) cutting the field to zero after t_w, and (4) recording the M_{TRM} magnetization decay as a function of time t. The TRM decay depends on T_m, t_w, and H_{fc}.

The TRM versus T_m experiments, performed on the Mn$_{0.3}$Ni$_2$Zn$_{10.7}$ γ-brass, are shown in Figure 7. A small field of $\mu_0 H_{fc} = 0.5$ mT was applied, and the aging stops were performed at eight different temperatures T_m between 16 and 2 K in steps of $\Delta T_m = 2$ K, where aging for $t_w = 1$ h was employed at each stop. After $H_{fc} \to 0$, the TRM decays were recorded up to $t \approx 150$ min. The normalized decays M_{TRM} $(T_m, t)/M_{fc}(T_m)$, where $M_{fc}(T_m)$ is the fc magnetization just before the field cutoff, are shown in Figure 7a, where an increase in amplitude with the decreasing T_m is evident. The inset shows the normalized initial ($t = 0$) amplitude $M_{TRM}(T_m, t = 0)/M_{fc}(T_m)$ as a function of T_m. The TRM at $T_m = T_f = 16$ K is zero, because the spin system is ergodic at that temperature. The decays slow down strongly with decreasing T_m, owing to an increased remanence of the spin system at lower temperatures. This is demonstrated in Figure 7b, where the TRM decays normalized to their $t = 0$ amplitudes, M_{TRM} $(T_m, t)/M_{TRM}(T_m, t = 0)$, are shown.

The TRM time decays versus the aging time t_w at $T_m = 8$ K, obtained after field cooling in $\mu_0 H_{fc} = 0.5$ mT, are presented in Figure 8. Eight different aging times between 1 min and 8 h, roughly logarithmically spaced, were employed. The normalized decay curves $M_{TRM}(t_w, t)/M_{fc}(t_w)$ are shown in Figure 8a. The TRM increases for longer t_w, which is additionally
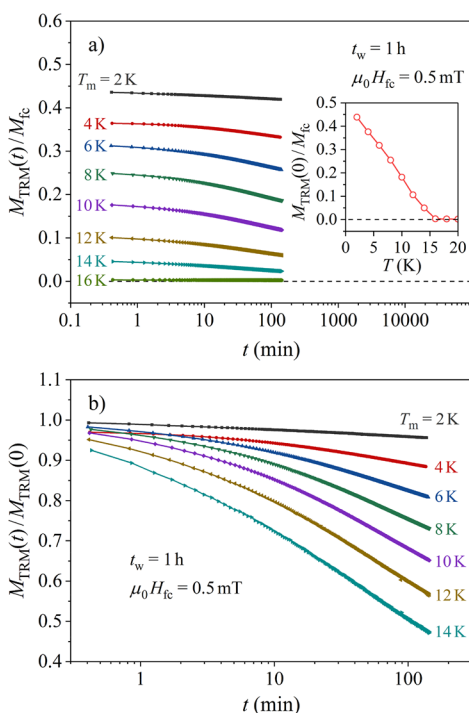
Figure 7. (a) Normalized TRM time-decay curves M_{TRM} $(T_m, t)/M_{fc}$ (T_m), at different temperatures T_m below $T_f \approx 16$ K. The normalized initial ($t = 0$) amplitude, M_{TRM} $(T_m, t = 0)/M_{fc}$ (T_m) as a function of T_m is shown in the inset. (b) Each curve is shown normalized to its $t = 0$ amplitude, M_{TRM} $(T_m, t)/M_{TRM}$ $(T_m, t = 0)$.
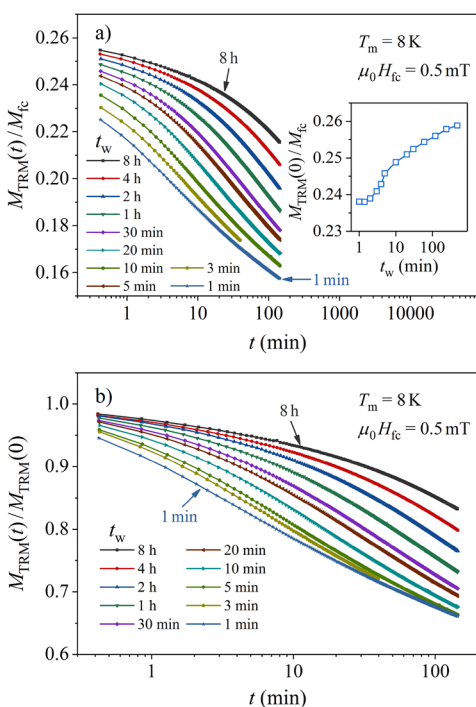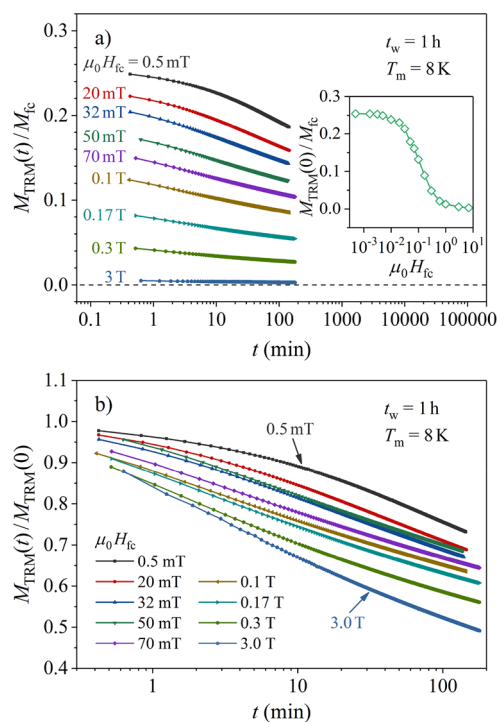

Figure 8. (a) Normalized TRM time-decay curves $M_{TRM}(t_w, t)/M_{fc}(t_w)$ as a function of the aging time t_w at $T_m = 8$ K. The normalized initial ($t = 0$) amplitude, $M_{TRM}(t_w, t = 0)/M_{fc}$ (t_w), as a function of t_w is shown in the inset. (b) Each curve is shown normalized to its $t = 0$ amplitude, $M_{TRM}(t_w, t)/M_{TRM}(t_w, t = 0)$.

demonstrated in the inset of Figure 8a, where the normalized initial ($t = 0$) TRM amplitude, $M_{TRM}(t_w, t = 0)/M_{fc}(t_w)$, is

shown as a function of t_w. The decay shapes also change with t_w, where a slowing-down for longer t_w values is evident. This is demonstrated in Figure 8b, where the TRM decays normalized to their $t = 0$ amplitudes, $M_{TRM}(t_w, t)/M_{TRM}(t_w, t = 0)$, are shown.

The TRM time decays versus the field H_{fc}, measured at $T_m = 8$ K for the aging time $t_w = 1$ h, are shown in Figure 9a. Fifteen


Figure 9. (a) Normalized TRM time-decay curves M_{TRM} $(H_{fc}, t)/M_{fc}$ (H_{fc}) vs the field H_{fc}, measured at $T_m = 8$ K for the aging time $t_w = 1$ h. The normalized initial ($t = 0$) amplitude M_{TRM} $(H_{fc}, t = 0)/M_{fc}$ (H_{fc}) as a function of H_{fc} is shown in the inset (note that the field scale is logarithmic). (b) Each curve is shown normalized to its $t = 0$ amplitude, M_{TRM} $(H_{fc}, t)/M_{TRM}$ $(H_{fc}, t = 0)$.

field values between $\mu_0 H_{fc} = 0.5$ mT and 7 T, roughly logarithmically spaced, were used. The normalized TRM time decays, M_{TRM} $(H_{fc}, t)/M_{fc}$ (H_{fc}), demonstrate a strong decrease of the TRM with increasing H_{fc}. The inset in Figure 9a shows the normalized initial ($t = 0$) TRM amplitude M_{TRM} $(H_{fc}, t = 0)/M_{fc}$ (H_{fc}), as a function of H_{fc}. A large decrease by 2 orders of magnitude within the investigated field range is evident. The change of the shape of the decay curves with H_{fc} is presented in Figure 9b, where each curve is shown normalized to its $t = 0$ amplitude, M_{TRM} $(H_{fc}, t)/M_{TRM}$ $(H_{fc}, t = 0)$. The decays show a tendency to slow down for smaller H_{fc} values.

Memory Effect. The memory effect (ME)[27,30,32−35] is another manifestation of the out-of-equilibrium, ultraslow dynamics of a nonergodic spin system, where the spin state formed upon isothermal aging can be retrieved after a reverse temperature cycle. The ME measurement protocol involves (1) continuous cooling of the spin system in a zero magnetic field through T_f into the nonergodic phase, (2) stopping at a certain temperature $T_{m1} < T_f$, and letting the system age isothermally for a macroscopic time t_w, ranging from a few minutes to many hours, (3) resuming the zero-field cooling after t_w, by performing eventually one or more additional consecutive aging stops at lower temperatures T_{mi}, (4)
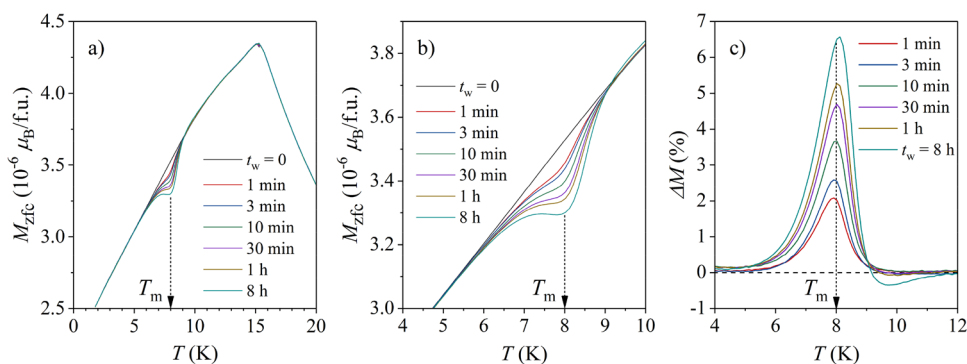
Figure 10. (a) M_{zfc} curves for different aging times t_w between 1 min and 8 h at $T_m = 8$ K. (b) M_{zfc}s in the region of T_m on an expanded scale. (c) The normalized difference $\Delta M = [M_{zfc}(t_w = 0) - M_{zfc}(t_w)]/M_{zfc}(t_w = 0)$.
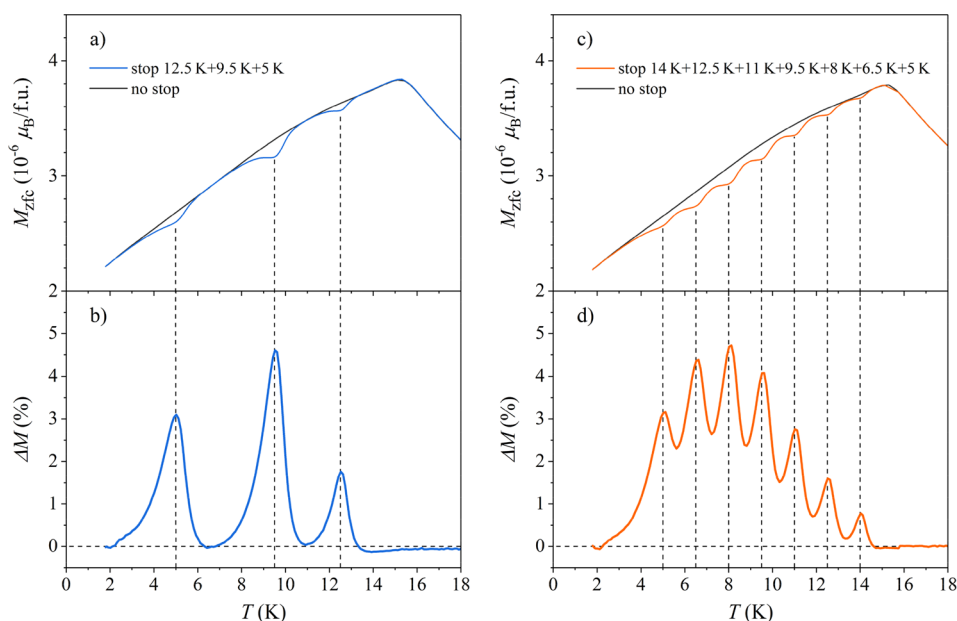
Figure 11. (a) M_{zfc} curve for three consecutive stops at $T_{m1} = 12.5$ K, $T_{m2} = 9.5$ K, and $T_{m3} = 5$ K for $t_w = 1$ h at each stop. The no-stop reference run is also presented. (b) Normalized difference ΔM, where three peaks at the T_{mi} values are evident. (c) M_{zfc} for seven consecutive stops at T_{mi} ($i = 1-7$) between 14 and 5 K separated by $\Delta T_{mi} = 1.5$ K and (d) the corresponding ΔMs.

applying a tiny magnetic field of the order $\mu_0 H = 0.1$ mT at the lowest temperature, and (5) recording the zfc magnetization M_{zfc} in a continuous heating run. The spin system remembers the isothermal aging periods at all stop temperatures T_{mi}, by showing a diminution (a dip) in the M_{zfc} at each T_{mi}, with respect to the no-aging case ($t_w = 0$). In addition to the aging temperatures, the spin system remembers also the duration t_w of each aging stop. By heating into the ergodic phase, all the memorized information is erased, and the spin system is the same as before aging, a phenomenon known as rejuvenation.

The ME on the $Mn_{0.3}Ni_2Zn_{10.7}$ γ-brass was performed by stopping at $T_{m1} = 8$ K and employing a series of aging times between $t_w = 1$ min and 8 h, approximately logarithmically spaced (each t_w was used in a separate experiment). A no-stop reference run ($t_w = 0$) was also performed. At 2 K (the lowest temperature of the cooling run), a field $\mu_0 H_{zfc} = 0.5$ mT was applied. The M_{zfc} values for all t_w values, measured when heated, are shown in Figure 10a, where a dip at T_{m1} in the aged curves is observed. The M_{zfc}s in the vicinity of T_{m1} are shown on the expanded scale in Figure 10b, where it is seen in more detail how the dip increases with the increasing t_w. The normalized difference between the reference ($t_w = 0$) curve and

the aged curves, $\Delta M = [M_{zfc}(t_w = 0) - M_{zfc}(t_w)]/M_{zfc}(t_w = 0)$, is shown in Figure 10c. ΔM is peaked at the aging temperature T_{m1} and increases in amplitude with t_w.

The ME involving multiple consecutive isothermal aging stops for $t_w = 1$ h within the same zfc cooling run was observed by performing three stops at $T_{m1} = 12.5$ K, $T_{m2} = 9.5$ K, and $T_{m3} = 5$ K. The no-stop reference run was also recorded. The corresponding M_{zfc}s are presented in Figure 11a, showing a dip at each T_{mi}. The normalized difference ΔM with three well-resolved peaks at T_{mi} is shown in Figure 11b. The M_{zfc}s for seven consecutive stops for $t_w = 1$ h each at the temperatures T_{mi} ($i = 1-7$) between 14 and 5 K in steps of $\Delta T_{mi} = 1.5$ K are shown in Figure 11c, whereas the corresponding ΔMs are shown in Figure 11d. All seven consecutive aging stops have been memorized by the nonergodic spin system.

3. DISCUSSION

Randomness, as one of the reasons responsible for the spin-glass behavior of the $Mn_{0.3}Ni_2Zn_{10.7}$ γ-brass, is emerging from the random distribution of diluted Mn moments at the OH sites, because Ni occupies the OT sites with the full occupancy of 1, and there is no randomness in the Ni sublattice. Another

source of randomness is the structural disorder caused by a partial occupancy of the CC and IT sites, though both sites are populated by nonmagnetic Zn. Here it is not clear whether both Mn and Ni ions possess sizable localized magnetic moments and participate in the spin-glass magnetism or only Mn is magnetic. A partial answer to this question can be derived from the specific heat study performed on the Ni_2Zn_{11} parent γ-brass,[22] which has revealed that no long-range magnetic ordering of Ni moments takes place down to 0.35 K. The reported C/T = 4.5 mJ mol^{-1} K^{-2} value in the $T \to 0$ limit can be attributed entirely to the electronic specific heat (the electronic specific heat coefficients of the Ni and Zn metals are γ_{Ni} = 7.04 mJ mol^{-1} K^{-2} and γ_{Zn} = 0.64 mJ mol^{-1} K^{-2}), so that there is no magnetic specific heat, suggesting that Ni ions do not possess sizable magnetic moments. Doping with a small amount of Mn is not expected to change significantly the magnetic state of Ni in the $Mn_{0.3}Ni_2Zn_{10.7}$ pseudobinary γ-brass, so it is reasonable to assume that the magnetism of the Mn-doped compound originates predominantly from the Mn ions. The diluted Mn moments are positioned randomly on the octahedral partial structure. The long-range oscillating RKKY interaction then frustrates the Mn spins, which are subjected to competing AFM/FM interactions, and a spin-glass state is consequently formed.

The magnetic state of the $Mn_{0.3}Ni_2Zn_{10.7}$ γ-brass exhibits broken-ergodicity phenomena below the spin-freezing temperature that are typical for spin glasses and other magnetically frustrated spin systems. The memory effect has already found an important technological application as a thermal memory cell for the thermal storage of digital information, in the absence of an electric, magnetic, or electromagnetic field.[36] The observed broken-ergodicity phenomena are not restricted to spin glasses but are present also in other nonergodic magnetically and electrically frustrated systems. A theoretical understanding of these out-of-equilibrium phenomena is still incomplete, because the experimentally measured physical quantities are frequency-dependent, depending on the frequency scale of the employed experimental observation technique. A comprehensive literature on the subject exists,[16,25−36] and for details, the reader is invited to consult those articles. Here we emphasize that the TRM and the ME in the $Mn_{0.3}Ni_2Zn_{10.7}$ γ-brass exhibit the same type of the T_m, t_w, and H_{fc} dependence as reported before for other spin systems belonging to the broad class of spin glasses, either diluted or concentrated, electrically conducting or insulating, site-disordered or site-ordered with geometric frustration. Such systems include canonical spin glasses,[16,27−30,33,34] geometrically frustrated quasicrystals,[31,37] and complex metallic alloys,[32] high-entropy alloys,[35,38,39] and magnetic nanoparticles.[40,41] The $Mn_{0.3}Ni_2Zn_{10.7}$ pseudobinary γ-brass can be classified as a spin glass, representing the first alloy from the family of γ-brasses belonging to this class.

4. CONCLUSIONS

The $Mn_xNi_2Zn_{11-x}$ (x = 0.1−0.5) pseudobinary γ-brass type phases were synthesized by a high-temperature synthesis. The crystal structures for two nonstoichiometric loading compositions x = 0.3 and 0.5 were determined by XRD and solved in the cubic space group $I\bar{4}3m$. Like the binary Ni_2Zn_{11} parent γ-brass, the structures are described by the 26-atom γ-cluster, distributed on a bcc lattice. The 8c(OT) and 24g(CO) sites of the γ-cluster are occupied solely by Ni and Zn, respectively, whereas the 12e(OH) site is Zn/Mn mixed populated. The

2a(CC) and 8c(IT) sites show a positional disorder, both being partially occupied by Zn. According to the space group type and the combination of chemical elements, the investigated $Mn_xNi_2Zn_{11-x}$ compounds belong to the I-cell γ-brasses from the group II.

It is worth mentioning that, due to the similar X-ray scattering factors of the constituent elements (Mn, Ni, and Zn), a site occupancy and substitution pattern could be accurately addressed by a combination of X-ray and neutron diffraction analyses. The neutron powder diffraction analysis of the γ-brass type pseudobinary phases will be the subject of our future investigations.

Magnetic properties were studied for the low-Mn loading composition of $Mn_{0.3}Ni_2Zn_{10.7}$. On the basis of the measurement of the temperature-dependent zfc and fc magnetization, the ac susceptibility, the $M(H)$ hysteresis curves, the thermoremanent magnetization, and the memory effect, we found that the spin system exhibits typical broken-ergodicity phenomena of a magnetically frustrated spin system below the spin-freezing temperature $T_f \approx 16$ K. Specific heat measurements support a kinetic spin-freezing transition. The above results allow a classification of the $Mn_{0.3}Ni_2Zn_{10.7}$ pseudobinary γ-brass as a spin glass.

5. EXPERIMENTAL SECTION

Samples of several loading compositions $Mn_xNi_2Zn_{11-x}$ (x = 0.1−0.5) were prepared from high-purity elements Mn (99.98%), Ni (99.99%), and Zn (99.999%) from Alfa Aesar. The amounts of elements were weighted according to the loading compositions and kept in one-end-closed silica tubes. The other ends of the ampules were sealed under high vacuum (pressure < 10^{-5} mbar). Sealed ampules were placed into a programmable furnace, which was heated to 600 °C at a rate of 2 °C/min, and then kept at that temperature for 24 h. After that, the samples were heated to 900 °C at a rate of 0.2 °C/min and annealed at that temperature for 6 h, followed by a cool-down to 450 °C at a rate of 0.1 °C/min. Next, they were annealed at that temperature for 107 h. A rapid cooling was then performed to 100 °C at a rate of 1.2 °C/min and kept at that temperature for 54 h. Finally, the furnace was turned off and left to cool naturally to room temperature.

The phase purity was verified for all samples by PXRD. A small fraction of each ingot was crushed and ground into a fine powder using an agate mortar and pestle. The PXRD data were collected at ambient temperature using a Rigaku MiniFlex 600 diffractometer (Bragg−Brentano geometry) with a 600 W X-ray tube (Cu Kα_1 radiation, λ = 1.540 56 Å) and D/teX Ultra silicon strip detector. The data were collected for the 2θ range from 10° to 80° with a step size of 0.02°. The JANA2006 program[42] was used to refine the PXRD data.

The structural model was elaborated from SCXRD data and analysis. Single crystals were selected from crushed ingots of the loading compositions $Mn_{0.3}Ni_{2.0}Zn_{10.7}$ and $Mn_{0.5}Ni_{2.0}Zn_{10.5}$, for which the PXRD patterns are shown in Figure 1. The crystals were glued to the tip of a glass fiber and mounted on the goniometer head. Each data set was collected at room temperature with a Bruker Photon II diffractometer equipped with graphite-monochromatic Mo Kα radiation (λ = 0.710 73 Å). The data reduction was performed by Apex III software. The structure solution and refinement were made by using the JANA2006 package program.[42]

An EDS analysis of the chemical composition was performed on Tungsten Environmental Scanning Electron Microscope ESEM Quanta 650 equipped with an Oxford Instruments Aztec Live Ultim Max SDD 40 mm2 EDS detection system.

Magnetic measurements were conducted on a Quantum Design MPMS3 magnetometer, equipped with a 7 T magnet and operating at temperatures between 1.8 and 400 K. The thermoremanent magnetization in low magnetic fields and the memory effect experiments were conducted using a copper AC/ULF coil of the

MPMS3 magnetometer to ensure an accurate and repeatable magnetic field. Prior to the low-field experiments, the Ultra-Low Field option was used to compensate for the residual magnetic field of the superconducting magnet. A needle-shaped sample of dimensions 5 × 1 × 1 mm³ was cut from the ingot and contained several differently oriented crystal grains. The long axis was parallel to the magnetic field, to minimize the demagnetization effect. The specific heat was measured on a Quantum Design Physical Property Measurement System (PPMS 9T), equipped with a 9 T magnet and operating in the temperature range between 1.9 and 400 K.

■ ASSOCIATED CONTENT

Accession Codes

CCDC 2078889−2078890 contain the supplementary crystallographic data for this paper. These data can be obtained free of charge via www.ccdc.cam.ac.uk/data_request/cif, or by emailing data_request@ccdc.cam.ac.uk, or by contacting The Cambridge Crystallographic Data Centre, 12 Union Road, Cambridge CB2 1EZ, UK; fax: +44 1223 336033.

■ AUTHOR INFORMATION

Corresponding Authors

Janez Dolinšek − *J. Stefan Institute, SI-1000 Ljubljana, Slovenia; Faculty of Mathematics and Physics, University of Ljubljana, SI-1000 Ljubljana, Slovenia;* Email: janez.dolinsek@ijs.si

Partha Pratim Jana − *Department of Chemistry, Indian Institute of Technology, 721302 Kharagpur, India;* orcid.org/0000-0002-1348-4150; Email: ppj@chem.iitkgp.ac.in

Authors

Sivaprasad Ghanta − *Department of Chemistry, Indian Institute of Technology, 721302 Kharagpur, India*

Anustoop Das − *Department of Chemistry, Indian Institute of Technology, 721302 Kharagpur, India*

Stanislav Vrtnik − *J. Stefan Institute, SI-1000 Ljubljana, Slovenia*

Darja Gačnik − *J. Stefan Institute, SI-1000 Ljubljana, Slovenia*

Jože Luzar − *J. Stefan Institute, SI-1000 Ljubljana, Slovenia*

Andreja Jelen − *J. Stefan Institute, SI-1000 Ljubljana, Slovenia*

Primož Koželj − *J. Stefan Institute, SI-1000 Ljubljana, Slovenia; Faculty of Mathematics and Physics, University of Ljubljana, SI-1000 Ljubljana, Slovenia*

Magdalena Wencka − *J. Stefan Institute, SI-1000 Ljubljana, Slovenia; Institute of Molecular Physics, Polish Academy of Sciences, PL-60-179 Poznań, Poland*

Complete contact information is available at:
https://pubs.acs.org/10.1021/acs.inorgchem.1c01418

Author Contributions

The manuscript was written through contributions of all authors. All authors have given approval to the final version of the manuscript.

Notes

The authors declare no competing financial interest.

■ ACKNOWLEDGMENTS

■ REFERENCES

(1) Dubois, J. M.; Belin-Ferré, E.; Feuerbacher, M.; Introduction to the science of complex metallic alloys. In *Complex Metallic Alloys: Fundamentals and Applications*; Dubois, J. M., Belin-Ferré, E., Eds.; Wiley-VCH Verlag GmbH & Co. KGaA: Weinheim, Germany, 2010.

(2) Steurer, W.; Dshemuchadse, J. *Intermetallics. Structures, Properties, and Statistics*; Oxford University Press: Oxford, UK, 2016.

(3) Mizutani, U. *Hume-Rothery Rules for Structurally Complex Alloy Phases*; CRC Press, Taylor & Francis Group: Boca Raton, FL, 2011.

(4) Mizutani, U.; Asahi, R.; Sato, H.; Takeuchi, T. The Hume-Rothery electron concentration rule for a series of gamma-brasses studied by full-potential linearized augmented plane wave (FLAPW). *Philos. Mag.* **2006**, *86*, 645−654.

(5) Mizutani, U.; Sato, H. The physics of the Hume-Rothery electron concentration rule. *Crystals* **2017**, *7*, 9.

(6) Mizutani, U.; Noritake, T.; Ohsuna, T.; Takeuchi, T. Hume-Rothery electron concentration rule across a whole solid solution range in a series of gamma-brasses in Cu-Zn, Cu-Cd, Cu-Al, Cu-Ga, Ni-Zn and Co-Zn alloy systems. *Philos. Mag.* **2010**, *90*, 1985−2008.

(7) Mizutani, U.; Inukai, M.; Sato, H. Hume-Rothery stabilisation mechanism and *d*-states-mediated Fermi surface-Brillouin zone interactions in structurally complex metallic alloys. *Philos. Mag.* **2011**, *91*, 2536−2542.

(8) Xie, W.; Miller, G. J. New Co-Pd-Zn γ-brasses with dilute ferrimagnetism and Co_2Zn_{11} revisited: Establishing the synergism between theory and experiment. *Chem. Mater.* **2014**, *26*, 2624−2634.

(9) Xie, W.; Liu, J.; Pecharsky, V.; Miller, G. J. γ-Brasses with spontaneous magnetization: Atom site preferences and magnetism in the Fe-Zn and Fe-Pd-Zn phase spaces. *Z. Anorg. Allg. Chem.* **2015**, *641*, 270−278.

(10) Ghanta, S.; Kamboj, R.; George, N. M.; Jana, P. P. Formation of γ-brass type pseudo-binary $Ni_2Zn_{11-4\delta}X_\delta$ ($0 \leq \delta \leq \sim 0.13$) (X = In and Ga) by an exchange mechanism. *J. Solid State Chem.* **2020**, *289*, 121465.

(11) Liang, J. L.; Du, Y.; Liao, C. Z.; Tang, Y. Y.; Nong, L. Q.; Zheng, F.; Xu, H. H. Experimental investigation on the phase equilibria of the Mn-Ni-Zn system at 400 °C. *J. Alloys Compd.* **2010**, *489*, 362−368.

(12) Ghanta, S.; Das, A.; Kamboj, R.; Jana, P. P. A partly disordered 2 × 2 × 2 - superstructure of γ-brass related phase in Mn-Ni-Zn system. *Z. Kristallogr. Z. Kristallogr. - Cryst. Mater.* **2021**, *236*, 71−80.

(13) Asahi, R.; Sato, H.; Takeuchi, T.; Mizutani, U. Interpretation of the Hume-Rothery electron concentration rule in the T_2Zn_{11} (T = Ni, Pd, Co, and Fe) γ brasses based on first-principles FLAPW calculations. *Phys. Rev. B: Condens. Matter Mater. Phys.* **2005**, *72*, 125102.

(14) Spanjers, C. S.; Dasgupta, A.; Kirkham, M.; Burger, B. A.; Kumar, G.; Janik, M. J.; Rioux, R. M. Determination of bulk and surface atomic arrangement in Ni-Zn γ-brass phase at different Ni to Zn ratios. *Chem. Mater.* **2017**, *29*, 504−512.

(15) Johansson, A.; Ljung, H.; Westman, S.; Norin, T. X-ray and neutron diffraction studies on Γ-Ni, Zn and Γ-Fe, Zn. *Acta Chem. Scand.* **1968**, *22*, 2743−2753.

(16) Binder, K.; Young, A. P. Spin glasses: Experimental facts, theoretical concepts, and open questions. *Rev. Mod. Phys.* **1986**, *58*, 801−976 and references therein.

(17) Selwood, P. V. *Magnetochemistry*; Interscience Publishers: New York, 1956; p 78.

(18) Mabbs, F. E.; Machin, D. J. *Magnetism and Transition Metal Complexes*; Chapman and Hall: London, UK, 1973; p 7.

(19) Coey, J. M. D. *Magnetism and Magnetic Materials*; Cambridge University Press: Cambridge, UK, 2010; pp 209−218.

(20) Mydosh, J. A. *Spin glasses: an experimental introduction*; Taylor & Francis: London, UK, 1993; p 67.

(21) Tari, A. *The Specific Heat of Matter at Low Temperatures*; Imperial College Press: London, UK, 2003; pp 167−174.

(22) Malik, Z.; Kneidinger, F.; Michor, H.; Puchegger, S.; Bauer, E.; Giester, G.; Rogl, P. Physical properties of non-centrosymmetric Ni_2Zn_{11}. *Intermetallics* **2013**, *38*, 88−91.

(23) Bouchaud, J.-P.; Cugliandolo, L. F.; Kurchan, J.; Mézard, M. Out of equilibrium dynamics in spin-glasses and other glassy systems. In *Spin Glasses and Random Fields*; Young, A. P.; Ed.; World Scientific: Singapore, 1997; pp 161−224.

(24) Kawashima, N.; Rieger, H. Recent progress in spin glasses. In *Frustrated Spin Systems*; Diep, H. T.; Ed.; World Scientific: Singapore, 2004; pp 491−586.

(25) Vincent, E.; Hammann, J.; Ocio, M.; Bouchaud, J.-P.; Cugliandolo, L. F. Slow dynamics and aging in spin glasses. In *Complex Behaviour of Glassy Systems. Lecture Notes in Physics*; Rubí, M.; Pérez-Vicente, C.; Eds.; Springer: Berlin, Germany, 1997; Vol. *492*, pp 184−219.

(26) Nordblad, P.; Svedlindh, P. Experiments on spin glasses. In *Spin Glasses and Random Fields*; Young, A. P.; Ed.; World Scientific: Singapore, 1997; pp 1−28.

(27) Bouchaud, J.-P.; Dupuis, V.; Hammann, J.; Vincent, E. Separation of time and length scales in spin glasses: Temperature as a microscope. *Phys. Rev. B: Condens. Matter Mater. Phys.* **2001**, *65*, 024439.

(28) Lederman, M.; Orbach, R.; Hammann, J. M.; Ocio, M.; Vincent, E. Dynamics in spin glasses. *Phys. Rev. B: Condens. Matter Mater. Phys.* **1991**, *44*, 7403−7412.

(29) Chu, D.; Kenning, G. G.; Orbach, R. Effect of magnetic fields on the relaxation of the thermoremanent magnetization in spin glasses. *Philos. Mag. B* **1995**, *71*, 479−488.

(30) Refregier, Ph; Vincent, E.; Hammann, J.; Ocio, M. Ageing phenomena in a spin-glass: effect of temperature changes below T_g. *J. Phys. (Paris)* **1987**, *48*, 1533−1539.

(31) Dolinšek, J.; Jagličić, Z.; Sato, T. J.; Guo, J. Q.; Tsai, A. P. Spin freezing in icosahedral Tb-Mg-Zn and Tb-Mg-Cd quasicrystals. *J. Phys.: Condens. Matter* **2003**, *15*, 7981−7996.

(32) Dolinšek, J.; Slanovec, J.; Jagličić, Z.; Heggen, M.; Balanetskyy, S.; Feuerbacher, M.; Urban, K. Broken ergodicity, memory effect, and rejuvenation in Taylor-phase and decagonal $Al_3(Mn,Pd,Fe)$ complex intermetallics. *Phys. Rev. B: Condens. Matter Mater. Phys.* **2008**, *77*, 064430.

(33) Jonason, K.; Vincent, E.; Hammann, J.; Bouchaud, J.-P.; Nordblad, P. Memory and chaos effects in spin glasses. *Phys. Rev. Lett.* **1998**, *81*, 3243−3246.

(34) Dupuis, V.; Vincent, E.; Bouchaud, J.-P.; Hammann, J.; Ito, A.; Katori, H. A. Aging, rejuvenation, and memory effects in Ising and Heisenberg spin glasses. *Phys. Rev. B: Condens. Matter Mater. Phys.* **2001**, *64*, 174204.

(35) Jelen, A.; Koželj, P.; Gačnik, D.; Vrtnik, S.; Krnel, M.; Dražić, G.; Wencka, M.; Jagličić, Z.; Feuerbacher, M.; Dolinšek, J. Collective magnetism of a single-crystalline nanocomposite FeCoCrMnAl high-entropy alloy. *J. Alloys Compd.* **2021**, *864*, 158115.

(36) Dolinšek, J.; Feuerbacher, M.; Jagodič, M.; Jagličić, Z.; Heggen, M.; Urban, K. A thermal memory cell. *J. Appl. Phys.* **2009**, *106*, 043917.

(37) Boulet, P.; de Weerd, M.-C.; Krnel, M.; Vrtnik, S.; Jagličić, Z.; Dolinšek, J. Structural model and spin-glass magnetism of the $Ce_3Au_{13}Ge_4$ quasicrystalline approximant. *Inorg. Chem.* **2021**, *60*, 2526−2532.

(38) Koželj, P.; Vrtnik, S.; Krnel, M.; Jelen, A.; Gačnik, D.; Wencka, M.; Jagličić, Z.; Meden, A.; Dražić, G.; Danoix, F.; Ledieu, J.; Feuerbacher, M.; Dolinšek, J. Spin-glass magnetism of the non-equiatomic CoCrFeMnNi high-entropy alloy. *J. Magn. Magn. Mater.* **2021**, *523*, 167579.

(39) Krnel, M.; Vrtnik, S.; Jelen, A.; Koželj, P.; Jagličić, Z.; Meden, A.; Feuerbacher, M.; Dolinšek, J. Speromagnetism and asperomagnetism as the ground states of the Tb-Dy-Ho-Er-Tm ≫ideal≪ high-entropy alloy. *Intermetallics* **2020**, *117*, 106680.

(40) Jönsson, P.; Hansen, M. F.; Nordblad, P. Nonequilibrium dynamics in an interacting Fe-C nanoparticle system. *Phys. Rev. B: Condens. Matter Mater. Phys.* **2000**, *61*, 1261−1266.

(41) Cador, O.; Grasset, F.; Haneda, H.; Etourneau, J. Memory effect and super-spin-glass ordering in an aggregated nanoparticle sample. *J. Magn. Magn. Mater.* **2004**, *268*, 232−236.

(42) Petříček, V.; Dušek, M.; Palatinus, L. Crystallographic computing system JANA2006: General features. *Z. Kristallogr. - Cryst. Mater.* **2014**, *229*, 345−352.